ACS APPLIED MATERIALS & INTERFACES

Research Article

www.acsami.org

Distribution of Crystalline Polymer and Fullerene Clusters in Both Horizontal and Vertical Directions of High-Efficiency Bulk Heterojunction Solar Cells

Chih-Ming Liu,[†] Ming-Shin Su,[†] Jian-Ming Jiang,[†] Yu-Wei Su,[†] Chun-Jen Su,[‡] Charn-Ying Chen,[§] Cheng-Si Tsao,[§] and Kung-Hwa Wei*[,†]

[†]Department of Materials Science and Engineering, National Chiao Tung University, 1001 Ta Hsueh Road, Hsinchu 30050, Taiwan, ROC

[‡]National Synchrotron Radiation Research Center, 101 Hsin-Ann Road, Science-Based Industrial Park, Hsinchu 30077, Taiwan, ROC

[§]Institute of Nuclear Energy Research, 1000 Wen-Hua Road, Longtan, Taoyuan 32546, Taiwan, ROC

Supporting Information

ABSTRACT: In this study, we used (i) synchrotron grazing-incidence small-/wide-angle X-ray scattering to elucidate the crystallinity of the polymer $PBTC_{12}TPD$ and the sizes of the clusters of the fullerenes $PC_{61}BM$ and $ThC_{61}BM$ and (ii) transmission electron microscopy/electron energy loss spectroscopy to decipher both horizontal and vertical distributions of fullerenes in $PBTC_{12}TPD$/fullerene films processed with chloroform, chlorobenzene and dichlorobezene. We found that the crystallinity of the polymer and the sizes along with the distributions of the fullerene clusters were critically dependent on the solubility of the polymer in the processing solvent when the solubility of fullerenes is much higher than that of the polymer in the solvent. In particular, with chloroform (CF) as the processing solvent, the polymer and fullerene units in the $PBTC_{12}TPD/ThC_{61}BM$ layer not only give rise to higher crystallinity and a more uniform and finer fullerene cluster dispersion but also formed nanometer scale interpenetrating network structures and presented a gradient in the distribution of the fullerene clusters and polymer, with a higher polymer density near the anode and a higher fullerene density near the cathode. As a result of combined contributions from the enhanced polymer crystallinity, finer and more uniform fullerene dispersion and gradient distributions, both the short current density and the fill factor for the device incorporating the CF-processed active layer increase substantially over that of the device incorporating a dichlorobenzene-processed active layer; the resulting power conversion efficiency of the device incorporating the CF-processed active layer was enhanced by 46% relative to that of the device incorporating a dichlorobenzene-processed active layer.

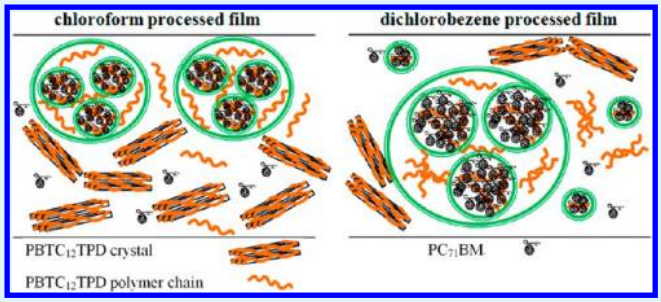

KEYWORDS: *bulk heterojunction solar cells, morphology, fullerenes, polymer crystallinity, grazing-incidence X-ray scattering, transmission electron microscopy*

1. INTRODUCTION

Great progress has been made recently in the development of organic photovoltaic devices incorporating active layers based on bulk heterojunction (BHJ) structures with conjugated polymers[1] as electron donors and nanometer-sized fullerenes as electron acceptors.[2−6] A complicated two-component BHJ active layer morphology that comprises phase-separated polymer-rich and fullerene-rich domains along with molecularly dispersed fullerenes and polymer chains typically arises from either their limited miscibility or large solubility disparity between polymer and fullerene in the processing solvent; their solubility is affected by the type of solvent, temperature, and other parameters employed during processing.[7−9] An active layer incorporating phase-separated nanometer-scale domains in a BHJ solar cell plays a critical role affecting the device performance because the interfaces between these domains provide a build-in electrical fields that allow the charge separation to take place for photogenerated excitons that diffuse to them; on the other hand, these polymer and fullerene domains also provide percolation pathways for holes and electrons, respectively, transport to the respective electrodes. The former requires a fine dispersion of fullerene units in the polymer for providing large interfaces because of the short exciton diffusion length (less than ten nanometers), whereas the latter necessities a suitable fullerene domain size to form pathways that can reduce a recombination of electrons and holes.[10] An optimal domain size as well as desirable distributions must be achieved for fullerenes in a polymer in

Received: October 3, 2012
Accepted: May 17, 2013
Published: May 17, 2013

   dx.doi.org/10.1021/am4011995 | ACS Appl. Mater. Interfaces 2013, 5, 5413−5422

order to obtain a high power conversion efficiency. The morphology of the active layer can be influenced to some extent by varying such parameters as the chemical composition,[11−17] the solvent used,[17,18] and the postprocessing treatment conditions,[19−28] but often it is not understood a priori. Particularly, the morphology of the active layer that critically determines the device efficiency is strongly affected by the processing solvents; a proper solvent can induce good polymer crystallinity if any and the optimized size of fullerene domains and their distribution, resulting in the best device performances. For probing the nanometer-scale domains of the active layer, only a few tools that can discriminate the small structure differences in polymer/fullerene composites can be adopted; among them, grazing-incidence X-ray scattering methods are most suitable for obtaining statistically meaningful structural information on hundreds-of-nanometers thick films.[8,12,13,22,28−33] Intricate characterization techniques such as state-of-the-art energy-filtered transmission electron microscopy (EFTEM)[34−36] are utilized for visualizing the a BHJ solar cell's active layer horizontal and cross-section morphology because conventional TEM show inherently little contrast.[37,38] One version of the EFTEM techniques is TEM with electron energy loss spectroscopy (EELS), TEM/EELS, which can be used to analyze the active layer in BHJ solar cell devices.

In this study, we have chosen poly-{bi(dodecyl)thiophene-dodecyl-thieno[3,4-*c*]pyrrole-4,6-dione} ($PBTC_{12}TPD$) with two different fullerenes, 1-(3-methoxycarbonyl)propyl-1-thienyl-(6,6)-methanofullerene ($ThC_{61}BM$) and $PC_{61}BM$, as the components for the active layers in the devices. We used synchrotron grazing-incidence small- and wide-angle X-ray scattering (GISAXS and GIWAXS) to elucidate the global morphology of $PBTC_{12}TPD$/fullerenes films and TEM/EELS with C-ratio to analyze the composition distribution of the cross section of the active layers processed with different solvents. Three processing solvents—chloroform (CF), chlorobenzene (CB), and 1,2-*o*-dichlorobenzene (DCB)— were used to dissolve $PBTC_{12}TPD$, $PC_{61}BM$, and $ThC_{61}BM$ in the quest to obtain the optimal morphology for the active layer. We intend to understand why the power conversion efficiency (PCE) improved from 4.2% for a device incorporating a DCB-processed $PBTC_{12}TPD/ThC_{61}BM$ (1:1.5, w/w) film as the active layer to 6.2%—a relative increase of 46%—for the corresponding device featuring CF-processed $PBTC_{12}TPD/ThC_{61}BM$ active layer.

2. EXPERIMENTAL SECTION

The synthesis of the conjugate polymer PBTTPD similar to that of the $PBTC_{12}TPD$ has been reported elsewhere;[39] $PC_{61}BM$ and $ThC_{61}BM$ were obtained from Solenne BV and the solvents CF, CB, and DCB from Sigma−Aldrich. All solutions of $PBTC_{12}TPD/PC_{61}BM$ and $PBTC_{12}TPD/ThC_{61}BM$ (30 mg/mL) were prepared at a $PBTC_{12}TPD$-to-$PC_{61}BM$ (or $ThC_{61}BM$) weight ratio of 1:1.5 at approximately 60 °C. The mixtures were spin-cast onto PEDOT:PSS−coated ITO glasses to provide an active layer of thickness of approximately 300 nm. Top contacts of Al (100 nm) were vacuum-deposited through thermal evaporation.

Photovoltaic measurements of the devices were performed under simulated AM 1.5G irradiation (100 mW/cm^2) using a Xe lamp−based Newport 66902 150-W solar simulator. A Xe lamp and an AM 1.5G filter were used as the white light source; the optical power at the position of the sample was 100 mW/cm^2. The *J*−*V* characteristics were measured using a Keithley 2400 source meter. External quantum efficiencies (EQEs) were measured using an SR150 (Optosolar, Germany) spectral response measurement setup.

Atomic force microscopy (AFM) images were recorded using a Digital Instruments Innova atomic force microscope operated at a scan rate of 1 Hz in tapping mode. TEM images were recorded using an FEI Tecnai G2 instrument operated at 120 keV. The samples for top-view TEM imaging were prepared in the same manner but at a thickness of 90 nm as the active layers used in the devices, followed by immersion in DI water for active layer exfoliation; the detached active layers were then transferred to a Cu foil for TEM imaging. The carbon elemental ratio was obtained using the standard two-energy-window method.[40]

GISAXS and GIWAXS measurements were performed at the SWAXS end station of the BL23A beamline of the Taiwan light source at the National Synchrotron Radiation Research Center (NSRRC). The BL23A beamline, equipped with a SAXS area detector and a WAXS area detector (in the meridian direction) connected to two data acquisition systems operated in master/slave mode, allowed GISAXS and GIWAXS measurements of correlated changes to the crystalline structures and nanostructures in the same probing area of the thin films of interest. The wave vector transfer Q was equal to $4\pi\sin(\theta/2)/\lambda$, defined in terms of the scattering angle θ and wavelength λ of the X-rays. The X-rays passed through a slit having a width of 0.5 mm; the photon energy was 8 keV; the sample-to-detector distances were 3 and 0.75 m for the GISAXS and GIWAXS systems, respectively; the angle of incidence was 0.2°. The samples were prepared on 4-cm^2 Si substrates through spin-coating of $PBTC_{12}TPD/PC_{61}BM$ and $PBTC_{12}TPD/ThC_{61}BM$ solutions; the film thickness was the same for each sample (ca. 300 nm).

3. RESULTS AND DISCUSSION

Figure 1a presents the molecular structures of the conjugated polymer $PBTC_{12}TPD$ and the two fullerene derivatives that we used to prepare the active layers in the devices. poly-{Bi(dodecyl)thiophene-dodecyl-thieno[3,4-*c*]pyrrole-4,6-dione}, $PBTC_{12}TPD$, featuring linear alkyl chains ($C_{12}H_{25}$) attached to thieno[3,4-*c*]pyrrole-4,6-dione ($C_{12}TPD$) units in conjugation with alkyl-bearing bithiophene (BT) units, was synthesized using a procedure similar to that reported previously for PBTTPD, which had branched alkyl chains attached to TPD units.[39] The TPD unit with different solubilizing groups that impacts the structural order and orientation in polymer backbones has been reported elsewhere;[39] it was found that the polymer having TPD units with linear alkyl chain gives higher molecular packing than that with branch alky chain. In the present study, we use the polymer that comproses TPD with linear alkyl chains, $PBTC_{12}TPD$, for allowing the polymers to crystallize easily in the presence of fullerenes. As fullerene derivatives, we used $PC_{61}BM$ and $ThC_{61}BM$, with the latter having higher electrical transport properties than those of the former.[41] Figure 1b presents X-ray diffraction curves of the CF-, CB-, and DCB-processed $PBTC_{12}TPD$ films; the peaks at 2.9, 5.9, and 8.9° indicate the diffraction from the (100), (200), and (300) plane of PBT $C_{12}TPD$ lamellae crystal, respectively, and a broad peak at 19.8°, corresponding to a distance of 4.5 Å, is assigned to the facial $\pi-\pi$ stacking of the lamellae.

Figure 1c presents UV−Vis absorption curves of films of $PBTC_{12}TPD$, $PC_{61}BM$, and $ThC_{61}BM$ that had been cast from CF solutions. The absorption peak at 470 nm for $PBTC_{12}TPD$ in CF solution resulted from internal charge transfer between the TPD acceptor and the BT donor; the solid $PBTC_{12}TPD$ film exhibited a maximum absorption near 550 nm—a significant red-shift of 80 nm relative to that in solution, indicating that considerably strong intermolecular interactions existed in the solid film. In addition, the vibronic shoulder at 650 nm implies an ordered arrangement of $PBTC_{12}TPD$

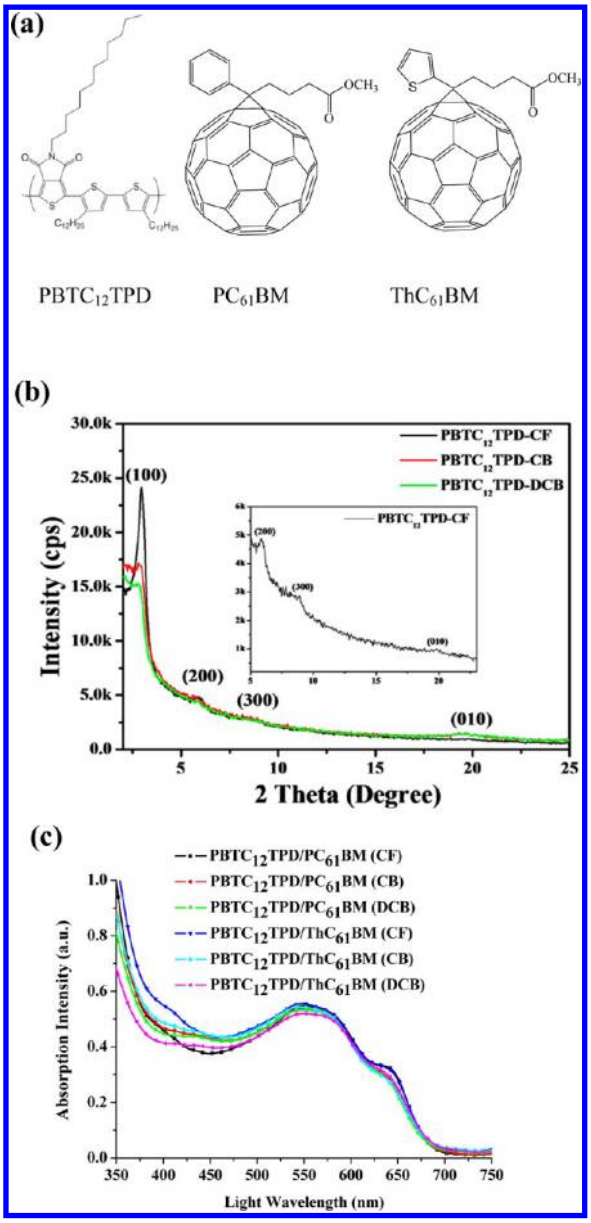

Figure 1. (a) Molecular structures of $PBTC_{12}TPD$, $PC_{61}BM$, and $ThC_{61}BM$. (b) X-ray diffraction curves of $PBTC_{12}TPD$ in CF, CB and DCB (c) Absorption spectra of $PBTC_{12}TPD$ (square), $PC_{61}BM$ (circle), and $ThC_{61}BM$ (triangle) films processed from CF and of $PBTC_{12}TPD$ in CF solution (inverted triangle). (c) Absorption spectra of $PBTC_{12}TPD/PC_{61}BM$ films processed from CF (square), CB (circle), and DCB (triangle) and of $PBTC_{12}TPD/ThC_{61}BM$ films processed from CF (inverted triangle), CB (rhombus), and DCB (left triangle).

molecules with strong $\pi-\pi$ stacking between the polymer backbones in the solid film, a feature that also appears in the film of regioregular poly(3-hexyl thiophene) (P3HT).[42,43] The absorption of $ThC_{61}BM$ in the range 300−400 nm was slightly higher than that of $PC_{61}BM$.

Figure 1d presents UV−vis absorption spectra of $PBTC_{12}TPD/PC_{61}BM$ and $PBTC_{12}TPD/ThC_{61}BM$ blend films spin-coated from CF, CB, and DCB solutions. Although these spectra featured almost the same absorption pattern regardless of the processing solvent, the absorption intensity in the range 350−450 nm for the $PBTC_{12}TPD/ThC_{61}BM$ film cast from CF was slightly stronger than that of the $PBTC_{12}TPD/PC_{61}BM$ film cast from CF. Additionally, the vibronic shoulders at 650 nm in the spectra of the CF-spun films were more pronounced than those in the spectra of the films cast from CB and DCB solutions, indicating more-ordered stacking for the CF-spun films. The UV−vis absorption spectra of $PBTC_{12}TPD/PC_{61}BM$ and $PBTC_{12}TPD/ThC_{61}BM$ blend films spin-coated from CF, CB, and DCB solutions were slightly blue-shifted as compared to that of the pristine $PBTC_{12}TPD$ film, possibly because of the fact that the size of the polymer crystallite reduced upon the addition of fullerenes.

Figure 2a and b reveal the photovoltaic performances of devices containing ca. 300 nm thick $PBTC_{12}TPD/PC_{61}BM$ and $PBTC_{12}TPD/ThC_{61}BM$ films, respectively, that had been processed using CF, CB, and DCB; Figure 2c lists the values of the open-circuit voltage (V_{oc}), short-current density (J_{sc}), and fill factor (FF) obtained from these curves. Although the

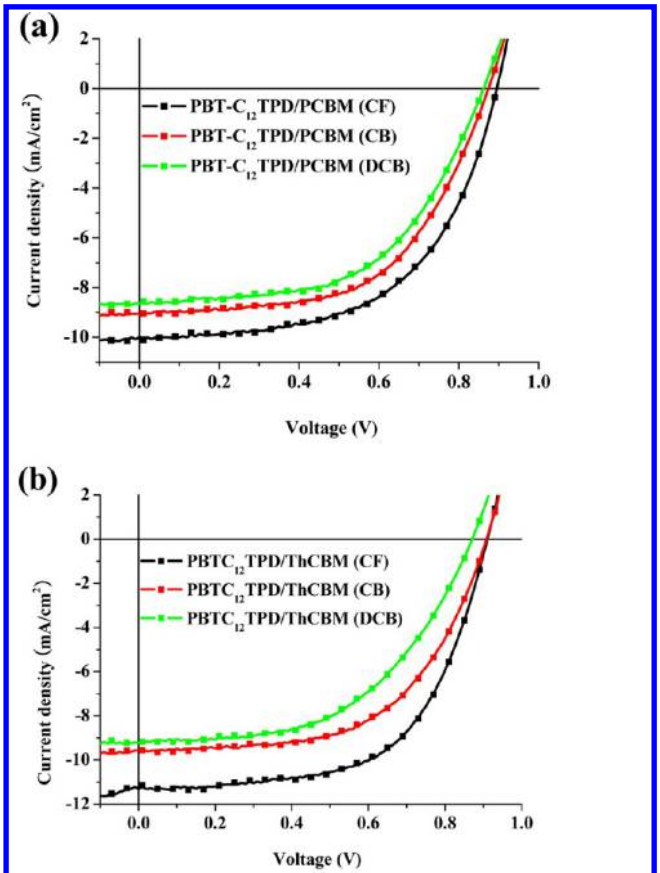

(c)

	$PBTC_{12}TPD/PC_{61}BM$				$PBTC_{12}TPD/ThC_{61}BM$			
Solvent	V_{oc} (V)	J_{sc} (mA/cm^2)	FF (%)	PCE[a] (%)	V_{oc} (V)	J_{sc} (mA/cm^2)	FF (%)	PCE[a] (%)
CF	0.9	9.9	57	*5.1*	0.91	11.3	60	*6.2*
CB	0.87	9	47	*4.5*	0.91	9.6	57	*5*
DCB	0.86	8.7	55	*4.1*	0.87	9.2	52	*4.2*

a) The PCE values of each devices are within an averaged error range of ±0.2% in ten measured devices.

Figure 2. Current density−voltage curves of (a) $PBTC_{12}TPD/PC_{61}BM$ and (b) $PBTC_{12}TPD/ThC_{61}BM$ films processed from CF, CB, and DCB. (c) Photovoltaic characteristics of devices incorporating $PBTC_{12}TPD/PC_{61}BM$ and $PBTC_{12}TPD/ThC_{61}BM$ active layers that were processed from CF, CB, and DCB.

dx.doi.org/10.1021/am4011995 | ACS Appl. Mater. Interfaces 2013, 5, 5413−5422

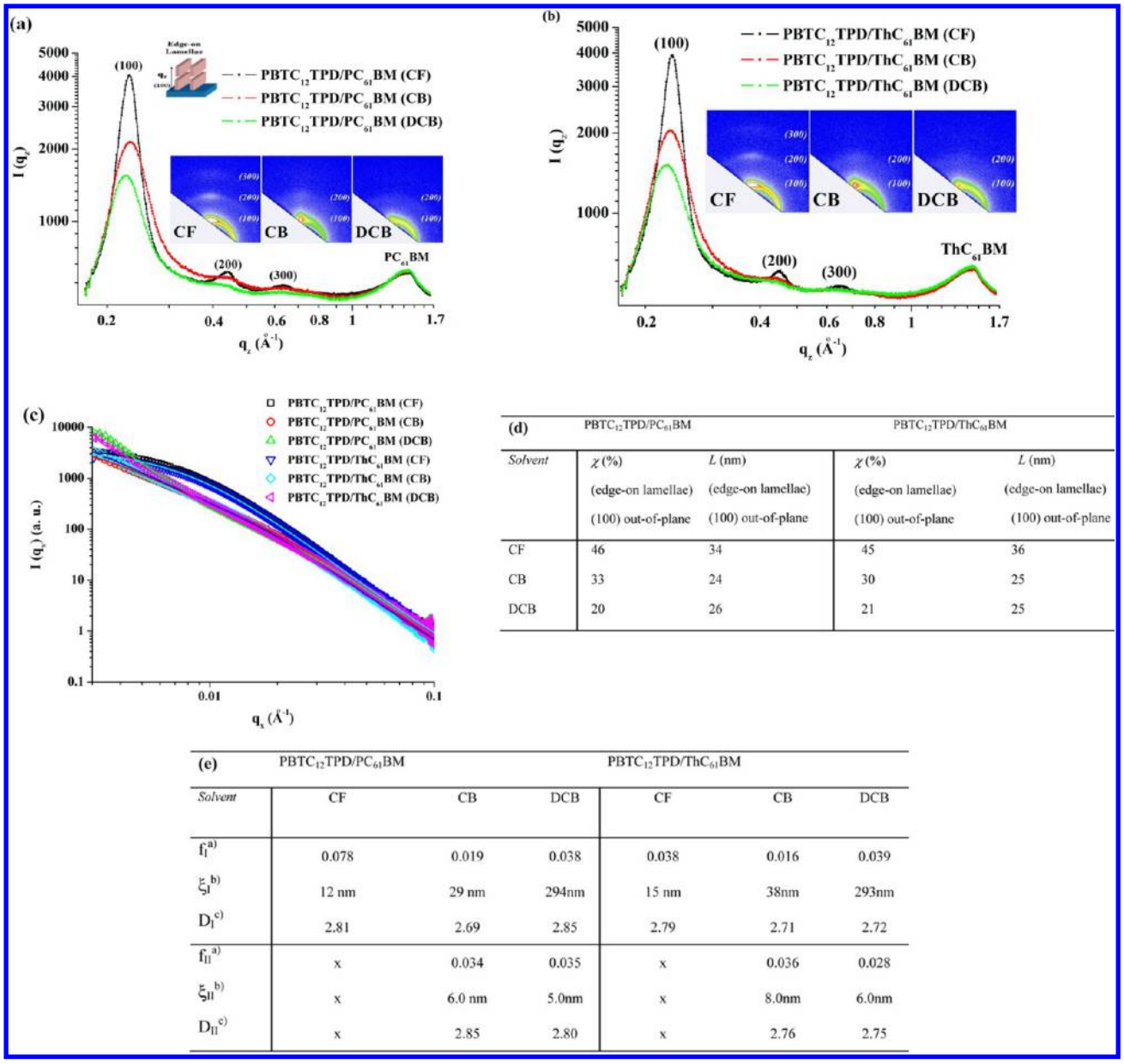

(d)

Solvent	PBTC$_{12}$TPD/PC$_{61}$BM χ (%) (edge-on lamellae) (100) out-of-plane	PBTC$_{12}$TPD/PC$_{61}$BM L (nm) (edge-on lamellae) (100) out-of-plane	PBTC$_{12}$TPD/ThC$_{61}$BM χ (%) (edge-on lamellae) (100) out-of-plane	PBTC$_{12}$TPD/ThC$_{61}$BM L (nm) (edge-on lamellae) (100) out-of-plane
CF	46	34	45	36
CB	33	24	30	25
DCB	20	26	21	25

(e)

Solvent	PBTC$_{12}$TPD/PC$_{61}$BM CF	CB	DCB	PBTC$_{12}$TPD/ThC$_{61}$BM CF	CB	DCB
$f_I^{a)}$	0.078	0.019	0.038	0.038	0.016	0.039
$\xi_I^{b)}$	12 nm	29 nm	294nm	15 nm	38nm	293nm
$D_I^{c)}$	2.81	2.69	2.85	2.79	2.71	2.72
$f_{II}^{a)}$	x	0.034	0.035	x	0.036	0.028
$\xi_{II}^{b)}$	x	6.0 nm	5.0nm	x	8.0nm	6.0nm
$D_{II}^{c)}$	x	2.85	2.80	x	2.76	2.75

Figure 3. Out-of-plane GIWAXS profiles of (a) PBTC$_{12}$TPD/PC$_{61}$BM and (b) PBTC$_{12}$TPD/ThC$_{61}$BM films spin-cast from CF, CB, and DCB solutions. The (100), (200), and (300) reflections of the PBTC$_{12}$TPD are indicated; the halos at $q_z \approx 1.4$ Å^{-1} correspond to the aggregation of fullerene derivatives (PC$_{61}$BM or ThC$_{61}$BM). (c) In-plane GISAXS profiles of PBTC$_{12}$TPD/PC$_{61}$BM and PBTC$_{12}$TPD/ThC$_{61}$BM films spin-cast from CF, CB, and DCB solutions. Data were fitted using a single fractal model for CF-processed films and a bifractal model for CB- and DCB-processed films to estimate the relative volume fraction and characteristic length of fractal system of PC$_{61}$BM or ThC$_{61}$BM clusters, and are shown in e. (d) Table for the relative crystallinity (χ) and the edge-on lamellae size (L) of the polymer estimated from the (100) reflections. (e) Table for the corresponding single and bifractal model fitted values of PC$_{61}$BM or ThC$_{61}$BM processed with CF, CB, and DCB.

open-circuit voltages of these devices were all similar (ca. 0.9 V), their short-circuit current densities were substantially different. For the devices incorporating the PBTC$_{12}$TPD/PC$_{61}$BM active layers, the values of J_{sc} ranged from 8.7 mA/cm^2 after DCB- and CB-processing to 9.9 mA/cm^2 after CF-processing. In contrast, the value of J_{sc} increased substantially to 11.3 mA/cm^2 for the device containing the CF-processed PBTC$_{12}$TPD/ThC$_{61}$BM active layer from 9.2 mA/cm^2 for the device containing the DCB-processed PBTC$_{12}$TPD/ThC$_{61}$BM active layer—an increase of greater than 20%. The values of measured J_{sc} in Figure 2c and those estimated from integrating the external quantum efficiency curves in Figure S1 in the Supporting Information were consistent (within an error range of 3%), confirming the accuracy of our measurements. The FF for the device containing the CF-processed PBTC$_{12}$TPD/ThC$_{61}$BM layer was 60%, 15% greater than that (52%) for the device containing the DCB-processed active layer. As a result of its enhanced values of J_{sc} and FF, the PCE of the device incorporating the CF-processed PBTC$_{12}$TPD/ThC$_{61}$BM layer (6.2%) was 46% higher than that (4.2%) of the devices incorporating the DCB-processed PBTC$_{12}$TPD/ThC$_{61}$BM layer. We suspected that the enhanced short-circuit current density and fill factor of the device incorporating the CF-processed PBTC$_{12}$TPD/ThC$_{61}$BM layer were due to its having a superior morphology relative to that of the DCB-processed PBTC$_{12}$TPD/ThC$_{61}$BM active layer. Moreover, the PCE of the

device incorporating the $PBTC_{12}TPD/ThC_{61}BM$ active layer was also higher than that of the $PBTC_{12}TPD/PC_{61}BM$ when processed with CF, 6.2 vs 5.1%. To decipher each component's distribution in the active layer of each BHJ device, we first used GIWAXS and GISAXS to deduce, from a global view, the degrees of crystallinity of the $PBTC_{12}TPD$ lamellae and the sizes of the aggregated fullerene clusters in the active layers.

Figure 3a and b present GIWAXS profiles taken along the out-of-plane direction, q_z, of approximately 300 nm thick $PBTC_{12}TPD/PC_{61}BM$ and $PBTC_{12}TPD/ThC_{61}BM$ (1:1.5, w/w) films, respectively; the insets display corresponding two-dimensional (2D) GIWAXS images. In the profile of the CF-processed $PBTC_{12}TPD/PC_{61}BM$ film in Figure 3a, the strong out-of-plane (100) peak at a value of q_z of 0.23 $Å^{-1}$ and the (200) and (300) peaks, respectively, represent scattering of the edge-on $PBTC_{12}TPD$ lamellae, which have an orientation in the out-of-plane direction of the film; the corresponding peak intensities for the CB- and DCB-processed $PBTC_{12}TPD/PC_{61}BM$ films were relatively weak. In Figure 3b, the same pattern appears in the GIWAXS profiles of the CF-, CB-, and DCB-processed $PBTC_{12}TPD/ThC_{61}BM$ films: the scattering of the edge-on $PBTC_{12}TPD$ lamellae formed from CF was much larger than those formed from CB and DCB. This feature indicates that the crystallinity of the $PBTC_{12}TPD$ lamellae in the CF-processed film was much larger than those in the CB- or DCB-processed films. Additionally, an amorphous halo at a value of q_z of 1.4 $Å^{-1}$, corresponding to short-range ordering of the $PC_{61}BM$ and $ThC_{61}BM$ clusters, appeared in the curves of all the films, regardless of the processing solvent. We estimated the corresponding polymer crystal sizes and the relative crystallinity from the (100) peak using the Scherrer equation and the integrated area under the peak, respectively.[8,12] Figure 3c displays the GISAXS profiles recorded along the in-plane direction, q_x, of the 2D images of CF-, CB-, or DCB-processed $PBTC_{12}TPD/PC_{61}BM$ and $PBTC_{12}TPD/ThC_{61}BM$ (1:1.5, w/w) films. Figure 3d summarizes the characteristics of the edge-on $PBTC_{12}TPD$ lamellae in the $PBTC_{12}TPD$/fullerene films. The crystallinity of the edge-on $PBTC_{12}TPD$ lamellae in the CF-processed $PBTC_{12}TPD/PC_{61}BM$ film was greater than those of the CB- and DCB-processed films by 1.4 and 2.3 times, respectively. Likewise, the CF-processed $PBTC_{12}TPD/ThC_{61}BM$ film also exhibited the similar higher crystallinity of its $PBTC_{12}TPD$ edge-on lamellae relative to those in the CB- and DCB-processed active layers. We estimated the $PBTC_{12}TPD$ (100) edge-on lamellar crystal sizes in the CF-processed $PBTC_{12}TPD/PC_{61}BM$ and $PBTC_{12}TPD/ThC_{61}BM$ films to be 34 and 36 nm, respectively; in contrast, for the CB- and DCB-processed $PBTC_{12}TPD/PC_{61}BM$ and $PBTC_{12}TPD/ThC_{61}BM$ films, the size was approximately 25 nm.

In the active layers, the domain size of fullerene aggregates can be determined by fitting the GISAXS profiles in Figure 3c with a choice of a proper fractal model. In some cases, a single fractal model such as I(q) = S(q)*F(q), where I, S, F and q are scattering intensity, structural factor, form factor and scattering vector, respectively, can be successfully used to fit the GISAXS profiles of polymer/fullerene blends; for instance, a single fractal model had been successfully used in our previous study[8] (see the Supporting Information for the analytical form) to fit the GISAXS profiles, providing a satisfactory interpretation of the morphology of the polymer/fullerene blend. In the present study, the GISAXS profiles of the CF-processed films can well be fitted with a single fractal model (Figure 3c). On the other hand, the GISAXS profiles of CB- and DCB-processed films exhibit similar curvature as that of the CF-processed films in the high-q region but display an upturn in the low-q region around 0.004 $Å^{-1}$, indicating the coexistence of two fractal structures-a small and a large structure. This leads us to try a few models that include a combination of a single fractal along with sphere or disk model for taking the larger structure into account to fit the GISAXS profiles in the CB and DCB cases, but without success. Using a bifractal model of $I(q) = \text{const}_1 S_1(q) F_1(q) + \text{const}_2 S_2(q) F_2(q)$, where const_1 and const_2 are related to the volume fraction of structure, we are able to successfully fit the GISAXS profiles of the CB- and DCB-processed films (Figure 3c), suggesting that two fractal structures with different characteristic lengths coexist in the system. The contrast between the bifractal model for CB and DCB cases to the single fractal model for CF case indicates that CF solvent induces a more uniform dispersion of fullerenes (Figure 3e) than CB and DCB solvent in the solid films in the presence of $PBTC_{12}TPD$.

The fitting result is shown in Figure 3e, where the $PBTC_{12}TPD/PC_{61}BM$ films that were processed with CB and DCB solvent possess two different fullerene fractal sizes, 6 and 29 nm for CB and 5 and 294 nm for DCB, respectively. Whereas, $PBTC_{12}TPD/PC_{61}BM$ films that were processed with CF have only one fullerene fractal size, 12 nm, indicating the better dispersion of fullerenes when processing with CF. The analytical form of the GISAXS intensity expressed by the scattering contrast and relative volume fraction is provided in the Supporting Information. Because the GISAXS measurement is not an absolute measurement, the true volume passed by the incident beam and electron contrast cannot be estimated, according to the current GISAXS reports. Moreover, these fitting parameters in the bifractal model are quite complicated. Therefore, the volume fraction and electron contrast-their product is the prefactor of intensity expression-can be considered only in the relative scale. The values of the same structural parameter for different solvent treatment, however, can be compared relatively. The relative volume fractions of different domain sizes in a film have different normalization factors.

These hierarchical fullerene structures for the CB- and DCB-processed films result from the much lower solubility of $PBTC_{12}TPD$ in CB and DCB than in CF, leading a poor dispersion of fullerenes in $PBTC_{12}TPD$. While the $PBTC_{12}TPD$ domains in the $PBTC_{12}TPD/PC_{61}BM$ and $PBTC_{12}TPD/ThC_{61}BM$ films exhibited approximately the same crystallinity (Figure 3d), the device data show a 14% difference in their short current density (9.9 vs 11.3 mA/cm^2), we speculate that the difference in the PCEs of the $PBTC_{12}TPD/PC_{61}BM$ (5.1%) and $PBTC_{12}TPD/ThC_{61}BM$ (6.2%) devices was caused primarily by (i) the higher absorption intensity in the range 350−450 nm for the $PBTC_{12}TPD/ThC_{61}BM$ film than that of the $PBTC_{12}TPD/PC_{61}BM$ film, (ii) the amount of their fullerene clusters with a decent size,[12,31] and (iii) higher intrinsic electrical conductivities for $ThC_{61}BM$.[41] From our GISAXS analyses, we conclude that the dispersed fullerene clusters in the CF-processed active layers containing $ThC_{61}BM$ possessed the optimal size,[12,31] 15 nm, and therefore, their active layer films possessed morphologies for superior charge transport than did those of the other films. Nevertheless, to better understand the morphologies in the blend systems, we used AFM to determine the surface morphologies. AFM images show that CF-processed films possessed more homogeneous morphology than CB and

DCB processed films either in $PC_{61}BM$ or $ThC_{61}BM$ systems (see the Supporting Information, Figure S2).

Figure 4a–c present top-view TEM images of $PBTC_{12}TPD/PC_{61}BM$ films that were spin-coated from CF, CB, and DCB

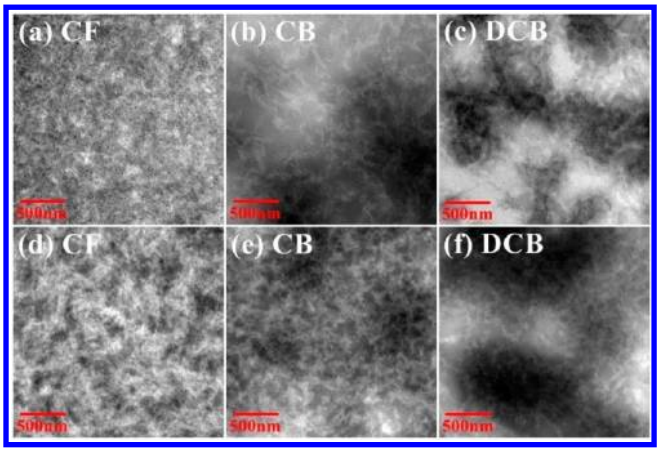

Figure 4. Top view TEM images of (a–c) $PBTC_{12}TPD/PC_{61}BM$ and (d–f) $PBTC_{12}TPD/ThC_{61}BM$ films processed from (a, d) CF, (b, e) CB, and (c, f) DCB, respectively.

solutions, respectively; Figure 4d–f present images of the corresponding $PBTC_{12}TPD/ThC_{61}BM$ films, respectively. The distinct bright and dark regions in these TEM images represent the conjugated polymer-rich and fullerene-rich domains, respectively, because the differences in the electron scattering densities of fullerenes (1.5 g/cm^3) and polymers (1.1 g/cm^3) are quite large. In the images of the DCB-processed $PBTC_{12}TPD/PC_{61}BM$ and $PBTC_{12}TPD/ThC_{61}BM$ films (Figure 4c, f) ,we observe domains of aggregated fullerene clusters having diameters of greater than 200 nm; in contrast, aggregated fullerene clusters having diameters of several tens of nanometers and forming an interpenetrating network structure with $PBTC_{12}TPD$ were evident in the image of the CF–spin-coated film in Figure 4d. Figure 4b and e reveal that the use of CB as the processing solvent led to aggregated fullerene clusters of intermediate size (ca. 100 nm) in the blend film. Moreover, the CF-, CB-, and DCB-processed $PBTC_{12}TPD/ThC_{61}BM$ films featured slightly larger aggregated fullerene clusters than did the corresponding $PBTC_{12}TPD/PC_{61}BM$ films. In comparing the fullerene domain sizes obtained from GISAXS and TEM results, there are some essential differences that must be accounted for even though they are complementary characterizing techniques. The TEM result provides a direct observation of structure sizes in a restricted region of the two-dimensional projection of polymer-rich and fullerene-rich domains that actually have three-dimensional shape. In contrast, GISAXS can gives independent interpretations for structures across different lengths in the form of fractal sizes and provide more details on the hierarchical structures that cannot well be distinguished with TEM. Hence, GISAXS and TEM results are consistent with each other within a certain length scale under careful comparisons. In our present study, the GISAXS data for CB-processed film revealed that the $ThC_{61}BM$ fractal size is about 38 nm; several $ThC_{61}BM$ fractals, however, may have aggregated into a larger domain where polymer chains intercalated between these fractals, resulting in a much larger domain, about 100 nm, that can be observed from TEM studies (TEM cannot well identify the interfaces between fractals). Therefore, our GISAXS results are consistent with our TEM observations.

These top-view TEM images provided the global horizontal directional active layer morphology; the charge transport pathways; however, depend critically on the blend film morphology in the vertical direction more so than the horizontal direction.[5,44–46] Therefore, we wished to also elucidate the morphologies of the active layers in their vertical direction to see whether they correlated with the photocurrents of the corresponding devices.

We prepared our samples for the TEM/EELS investigations with processing condition similar to those used for device fabrication, so that the deduced morphology could be related directly to the performance of polymer BHJ solar cells, and then used the focused ion beam (FIB) technique to prepare thin slices of cross sections of the devices, which had the configuration Al/active layer/PEDOT:PSS/ITO/glass, with a thin layer of Ti coated on the top of the device to protect it from damage during FIB thin sectioning. Images a and d in Figure 5a and d display the cross-sectional BF TEM images of

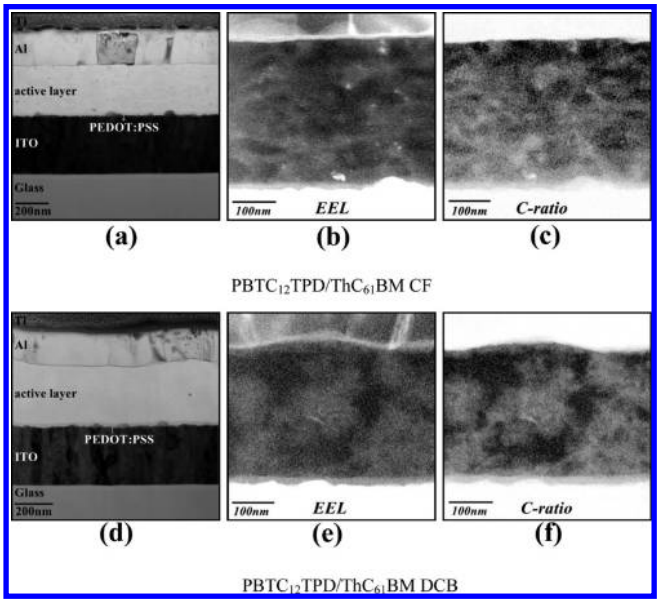

Figure 5. (a, d) Cross-sectional, (b, e) EEL, and (c, f) C-ratio TEM images of $PBTC_{12}TPD/ThC_{61}BM$ films processed from (a–c) CF and (d–f) DCB.

the CF- and DCB-processed $PBTC_{12}TPD/ThC_{61}BM$ films, respectively; as expected, no appreciable contrast can be observed in the active layers, whereas the cross-sectional EEL TEM images of the active layers in Figure 5b and e reveal varying contrasts along the vertical direction, due to phase separation in blend film, as expected from the EEL measurements. In general, the low-EEL range of TEM can be used to distinguish between conjugated polymer and $PC_{61}BM$ domains, due to the fact that the positions of the EEL peaks of conjugated polymers and fullerenes typically appear near 26 and 29 eV,[36] respectively. At an energy level of 29 eV, the contrast between the polymer- and fullerene-rich domains was optimized, generating dark and bright images, respectively. Here, we have inverted the images of these polymer- and fullerene-rich domains in EEL TEM to bright and dark images, respectively, so that we can compare them directly with the BF TEM images, which feature bright polymer-rich domains and

dark fullerene-rich domains. Figure 5c and f present cross-sectional C-ratio TEM images, with the C-ratio defined as the integrated area of the carbon atomic absorption energy (ca. 284 eV) window after subtracting the relative background energy area or carbon density distribution. Similar to the TEM EEL images, we have also inverted these cross-sectional C-ratio TEM images so that bright and dark regions correspond to $PBTC_{12}TPD$-rich and $ThC_{61}BM$-rich domains, respectively; the dark regions indicate a high C-ratio intensity, due to the higher carbon density of the aggregated fullerene derivatives. The C-ratio TEM image of the CF-cast $PBTC_{12}TPD/ThC_{61}BM$ film revealed a fine interpenetrated network morphology; in contrast, that the image of the DCB-cast $PBTC_{12}TPD/ThC_{61}BM$ film revealed a gross phase-separated morphology.

Figure 6a and b present the profiles of the C-ratio TEM images along the vertical direction for the CF- and DCB-cast

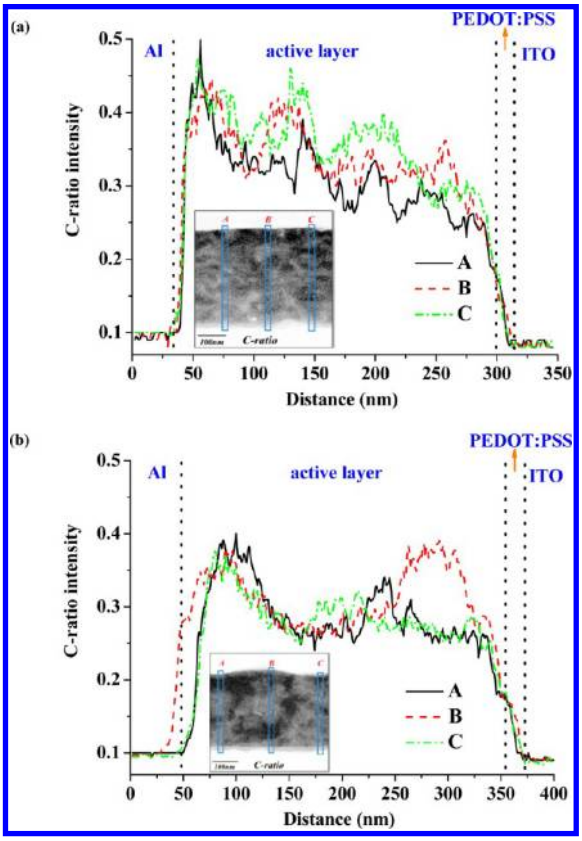

Figure 6. Cross-sectional EEL and C-ratio TEM images of $PBTC_{12}TPD/ThC_{61}BM$ films processed from (a) CF and (b) DCB.

$PBTC_{12}TPD/ThC_{61}BM$ films, respectively. All three of the C-ratio profiles (each spanning 200 nm) of the active layer in Figure 6a reveal a small oscillating C-ratio intensity with a gradient that has the highest intensity near the Al electrode and lowest intensity near the PEDOT:PSS/ITO electrode. This gradient in the C-ratio implies that proportionally more aggregated fullerene clusters existed near the Al electrode (cathode) and that more conjugated polymer-rich regions existed near the PEDOT:PSS/ITO electrode (anode). This composition gradient distribution is that of an ideal active layer structure: fullerene clusters near the cathode would benefit electron transport to the cathode and conjugated polymer domains near the anode would benefit hole transport to the anode.[5] On the other hand, although the three C-ratio profiles of the DCB-processed $PBTC_{12}TPD/ThC_{61}BM$ film displayed similar oscillation amplitudes, each possessed either a bimodal distribution or a flat distribution across the active layer, indicating no preferable fullerene cluster distribution. These profiles revealed that the active layer of the DCB-cast $PBTC_{12}TPD/ThC_{61}BM$ film featured large (ca. 100 nm) aggregates of the fullerene derivative, but with no specific distributions of the conjugated polymer and fullerene derivatives near the cathode and anode. In contrast to the conventional thinking that a high boiling point solvent such as CB or DCB for processing the active layer materials usually gave a better dispersion of fullerenes in the polymer than a low boiling point processing solvent such as in the case of P3HT with PCBM, this case is different due to the solubility difference between $PBTC_{12}TPD$ and fullerenes in the solvents. First, these two solvents, CF and DCB, show small difference in dissolving fullerenes below the 3 wt % solution concentration at which the active layer solution was processed. Therefore, the main determining factor for such different morphology lies in the large disparity in the solubility of $PBTC_{12}TPD$ in CF and in DCB, particularly with respect to the temperature change; $PBTC_{12}TPD$ has much higher solubility in hot CF than in hot CB or DCB but is prone to crystallization once the temperature of the solution decreased and become highly crystalline in the solid state without solvent or thermal annealing.

Specifically, we have carried out experiments for discerning the solubility of $PBTC_{12}TPD$ in CF, CB and DCB quantitatively at room temperature based on the specifications of ASTM E1148; the results are listed in Table 1. Table 1

Table 1. Solubility of $PBTC_{12}TPD$ and $ThC_{61}BM$ in Chloroform (CF), Chlorobenzene (CB), and 1,2-*o*-Dichlorobenzene (DCB) at Room Temperature Determined Following ASTM E1148

solvent	$PBTC_{12}TPD$ (mg mL^{-1})	$ThC_{61}BM$ (mg mL^{-1})
CF	4.5	26.3
CB	2.0	34.7
DCB	0.5	14.1

shows that the solubility of $PBTC_{12}TPD$ in CF at room temperature is much greater than that in CB or DCB—4.5 vs 2.0 or 0.5 mg per mL. We used 3 wt % $PBTC_{12}TPD/ThC_{61}BM$ (w/w, 1:1.5) solutions that consist of 1.2 wt % $PBTC_{12}TPD$ and 1.8 wt % $ThC_{61}BM$ in the solutions for the active layer processing. The solubilities of $ThC_{61}BM$ in CF and in CB at room temperature are quite high—26 and 34 mg per mL, respectively, whereas the solubility of $ThC_{61}BM$ in DCB is 14 mg per mL. At the elevated temperatures such as 60 °C, however, we expect that the 1.8 wt % $ThC_{61}BM$ (about 18 mg per mL) will be completely soluble, regardless of which one of the three solvents is used, and therefore focus more on the solubility study of $PBTC_{12}TPD$.

Figure 7 show the small-angle X-ray scattering (SAXS) profiles for $PBTC_{12}TPD$ in CF and DCB at a concentration of 1.2 wt % (about 12 mg/mL) at 20, 40 and 60 °C, respectively. The presence of scattering peaks at scattering vector q = 0.18 $Å^{-1}$ for $PBTC_{12}TPD$ in both CF and DCB at 20 and 40 °C indicated that there are domains of aggregated $PBTC_{12}TPD$ molecules present—they are not completely soluble in CF or DCB at 20 and 40 °C. SAXS scattering profiles of the polymer solution exhibit a peak in high-q region (0.18 $Å^{-1}$) that account

dx.doi.org/10.1021/am4011995 | ACS Appl. Mater. Interfaces 2013, 5, 5413−5422

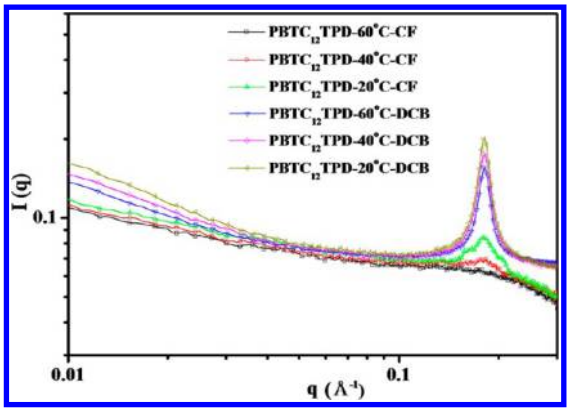

Figure 7. Small-angle X-ray scattering profile of 1.2 wt % $PBTC_{12}TPD$ in CF and DCB solution at 20, 40, and 60 °C, respectively.

for the domain comprising aggregated polymer chains intercalated with solvent molecules. Whereas, thin film GIXD only provide information on the crystallized polymer domain, and the resulting diffraction peak at q of 0.23 $Å^{-1}$ indicates a much smaller structure.

The intensity of the scattering peak for $PBTC_{12}TPD$ in DCB is much greater than that in CF, indicating a large solubility disparity of $PBTC_{12}TPD$ in CF and in DCB, which is consistent with the solubility data in Table 1. As the temperature increased to 60 °C, the solubility of $PBTC_{12}TPD$ increased more prominently in CF than in DCB, as evidenced by the larger reduction in the scattering peak intensity in the case of CF than in the case of DCB. The SAXS profile of 1.2 wt % $PBTC_{12}TPD$ in CF at 60 °C did not show any peak indicates almost complete solubility while the scattering peak being still present for the case of $PBTC_{12}TPD$ in DCB. Therefore, the solubility of $PBTC_{12}TPD$ in CF not only is better than that in DCB but also is more sensitive to the temperature changes from 60 to 20 °C, in which temperature range the active layers were processed. On the other hand, the $ThC_{61}BM$ display much better solubility in CF than in DCB. Therefore, both $PBTC_{12}TPD$ and $ThC_{61}BM$ can be dissolved much better in CF than in DCB, and therefore their interaction and domain sizes are much better and finer, respectively, in CF than in DCB.

Figure 8a and b show the cartoon images of the $PBTC_{12}TPD/ThC_{61}BM$ (w/w, 1:1.5) solutions state in CF and DCB solvent, respectively, based on the solubility, solution SAXS data, and Figure 8c and d show the schematic drawings of the cross-sectional view of the active layer morphology processed with CF and DCB, respectively, based on the results of GIWAXS, GISAXS and TEM analyses. Typically, after spin-coating of the polymer/fullerene active layer solution at elevated temperature, the active layer morphology evolves and forms through the competition[30] between aggregating fullerenes and crystallizing polymers, if any. When the active layer solution temperature decreases from 60 °C to room

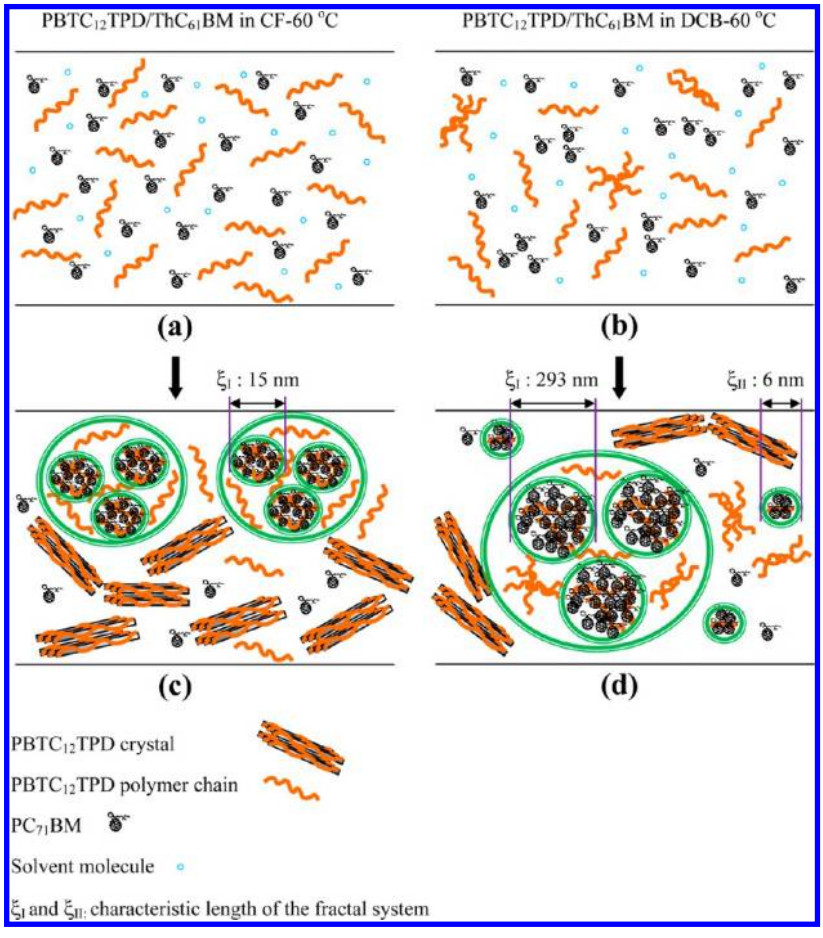

Figure 8. Cartoon images (not to the scale) of $PBTC_{12}TPD/ThC_{61}BM$ solution state in (a) CF and (b) DCB solvent at 60 °C and of cross-sectional view of film processed from (c) CF and (d) DCB solvent.

dx.doi.org/10.1021/am4011995 | ACS Appl. Mater. Interfaces 2013, 5, 5413−5422

temperature, there are more $PBTC_{12}TPD$ molecules available for crystallization (aggregated polymers cannot crystallize well) along with more fullerene molecules remaining soluble in the CF than in the DCB case, and the fact that $PBTC_{12}TPD$ is more sensitive to the temperature changes indicates that more $PBTC_{12}TPD$ molecules can crystallize without the interference of the fullerene domains that remain soluble in the solution, resulting in much less constraints on the growth of the size of the $PBTC_{12}TPD$ crystal lamellae. Hence, both the crystallinity and the size of edge-on $PBTC_{12}TPD$ lamellae crystal are larger, and the fullerene domain in turn is constrained by the edge-on $PBTC_{12}TPD$ lamellae crystal and becomes finer in the solid film than that in the film processed with DCB. Additionally, the fact that there are more $PBTC_{12}TPD$ available for crystallization, and $PBTC_{12}TPD$ crystallize much faster than the $ThC_{61}BM$ aggregate induces the formation of a higher polymer density near the anode after solvent evaporated in the CF case, forming a gradient distribution. Whereas, in the DCB case, at the room temperature the deposition of the aggregated $PBTC_{12}TPD$ and slightly aggregated $ThC_{61}BM$ domains onto the PEDOT:PSS layer take place more equally—they have about equal probability to deposit onto the PEDOT:PSS layer.

As a result, both the $PBTC_{12}TPD$ crystallinity and the size of edge-on lamellae crystal in the active are smaller and the size of the fullerene domain is larger in the DCB case than those in the case of CF solvent, resulting in a bimodal distribution across the active layer. Hence, in the case of large differences in solubility of the polymer in the processing solvent and the high sensitivity of the solution toward temperature changes, a low boiling point processing solvent such as CF (bp 61 °C) can give better results than a boiling point processing solvent such as DCB (bp 181 °C) for obtaining the optimum morphology.

Although the vertical distribution effect is a minor parameter[47] to determine the device performance for some cases, it undoubtedly further enhances the device performance. On the basis of the GIWAXS and GISAXS results along with the cross-sectional TEM images, we can explain the optimal device performance obtained from the CF-processed active layer by considering that (i) the higher polymer crystallinity, (ii) finer and more uniform fullerene domain size in the active layer, and (iii) its nanometer scale interpenetrating and gradient distribution network structures, which provided favorable pathways for charge transport. As a result, the performance of the device incorporating the CF-cast $PBTC_{12}TPD/ThC_{61}BM$ film was 46% higher than that of the corresponding device incorporating the DCB-cast film.

4. CONCLUSIONS

We have used both GISAXS/GIWAXS and TEM low-EEL imaging along with C-ratio profiling to elucidate the morphology that includes the cross-sectional distributions of the polymer and fullerene in $PBTC_{12}TPD/ThC_{61}BM$ films. We have found that the morphology and the distributions of the fullerene fractals and polymers could vary widely and were critically affected by the nature of the processing solvent when the solubility of the polymer varies greatly in the solvents. In particular, with CF as the processing solvent, the crystallinity of the $PBTC_{12}TPD$ in the $PBTC_{12}TPD/PC_{61}BM$ film was greater and the domain of fullerene clusters was more uniform and finer than those of the CB- and DCB-processed films because the polymer crystallizes much faster than the fullerenes aggregate in CF processed film. In addition, $PBTC_{12}TPD/ThC_{61}BM$ active layer structure processed with CF proportionally more aggregated fullerene clusters existed near the cathode and that more conjugated polymer-rich regions existed near the anode that obtained using DCB. As a result of combined contributions from the enhanced polymer crystallinity, finer fullerene dispersion and their gradient distributions, the power conversion efficiency of the device incorporating the CF-processed active layer was enhanced by 46% relative to that of the device incorporating a dichlorobenzene-processed active layer.

■ ASSOCIATED CONTENT

Supporting Information

EQE curves of devices containing $PBTC_{12}TPD/PC_{61}BM$ and $PBTC_{12}TPD/ThC_{61}BM$ films processed from CF, CB, and DCB solutions displayed in Figure S1. Figure S2 presents AFM height and phase images of the $PBTC_{12}TPD/PC_{61}BM$ and $PBTC_{12}TPD/ThC_{61}BM$ films processed with CF, CB, and DCB. Figure S3 presents GISAXS patterns of the $PBTC_{12}TPD/PC_{61}BM$ and $PBTC_{12}TPD/ThC_{61}BM$ films processed with CF, CB, and DCB. The Guinier approximation was used to determined radius of gyration (R_g) of a fullerene cluster. Figure S4 show the measured GISAXS profiles of the $PBTC_{12}TPD/PC_{61}BM$ and $PBTC_{12}TPD/Th_{61}BM$ processed with different solvents modeled with by a single fractal and bifractal models. This material is available free of charge via the Internet at http://pubs.acs.org.

■ AUTHOR INFORMATION

Corresponding Author

*E-mail: khwei@mail.nctu.edu.tw. Tel: 886-3-5712121 ext 31871. Fax: 886-3-5724727.

Notes

The authors declare no competing financial interest.

■ ACKNOWLEDGMENTS

We thank Dr. U.S. Jeng for the discussing of the small-angle X-ray scattering experiments. We also thank the National Science Council for financial support (NSC 101-3113-P-009-005).

■ REFERENCES

(1) Jiang, J. M.; Yuan, M. C.; Dinakaran, K.; Hariharanb, A.; Wei, K. H. *J. Mater. Chem. A* **2013**, *1*, 4415−4422.
(2) Thompson, B. C.; Fréchet, J. M. J. *Angew. Chem., Int. Ed.* **2008**, *47*, 58−77.
(3) Chen, L. M.; Xu, Z.; Honga, Z.; Yang, Y. *J. Mater. Chem.* **2010**, *20*, 2575−2598.
(4) Peet, J.; Senatore, M. L.; Heeger, A. J.; Bazan, G. C. *Adv. Mater.* **2009**, *21*, 1521−1527.
(5) Hoppe, H.; Sariciftci, N. S. *J. Mater. Chem.* **2006**, *16*, 45−61.
(6) Su, Y. W.; Lan, S. C.; Wei, K. H. *Mater. Today* **2012**, *15*, 554−562.
(7) Lee, J. K.; Ma, W. L.; Brabec, C. J.; Yuen, J.; Moon, J. S.; Kim, J. Y.; Lee, K.; Bazan, G. C.; Heeger, A. J. *J. Am. Chem. Soc.* **2008**, *130*, 3619−3623.
(8) Su, M. S.; Kuo, C. Y.; Yuan, M. C.; Jeng, U. S.; Su, C. J.; Wei, K. H. *Adv. Mater.* **2011**, *23*, 3315−3319.
(9) Amb, C. M.; Chen, S.; Graham, K. R.; Subbiah, J.; Small, C. E.; So, F.; Reynolds, J. R. *J. Am. Chem. Soc.* **2011**, *133*, 10062−10065.
(10) Nelson, J.; Kwiatkowski, J. J.; Kirkpatrick, J.; Frost, J. M. *Acc. Chem. Res.* **2009**, *42*, 1768−1778.
(11) Bavel, S. S.; Barenklau, M.; With, G.; Hoppe, H.; Loos, J. *Adv. Funct. Mater.* **2010**, *20*, 1458−1463.
(12) Chiu, M. Y.; Jeng, U. S.; Su, M. S.; Wei, K. H. *Macromolecules* **2010**, *43*, 428−432.

(13) Lilliu, S.; Agostinelli, T.; Pires, E.; Hampton, M.; Nelson, J.; Macdonald, J. E. *Macromolecules* **2011**, *44*, 2725−2734.
(14) Rance, W. L.; Ferguson, A. J.; McCarthy-Ward, T.; Heeney, M.; Ginley, D. S.; Olson, D. C.; Rumbles, G.; Kopidakis, N. *ACS Nano* **2011**, *5*, 5635−5646.
(15) Yu, B. Y.; Lin, W. C.; Wang, W. B.; Iida, S. I.; Chen, S. Z.; Liu, C. Y.; Kuo, C. H.; Lee, S. H.; Kao, W. L.; Yen, G. J.; You, Y. W.; Liu, C. P.; Jou, J. H.; Shyue, J. J. *ACS Nano* **2010**, *4*, 833−840.
(16) Keivanidis, P. E.; Clarke, T. M.; Lilliu, S.; Agostinelli, T.; Macdonald, J. E.; Durrant, J. R.; Bradley, D. D. C.; Nelson, J. *J. Phys. Chem. Lett.* **2010**, *1*, 734−738.
(17) Barrau, S.; Andersson, V.; Zhang, F.; Masich, S.; Bijleveld, J.; Andersson, M. R.; Inganas, O. *Macromolecules* **2009**, *42*, 4646−4650.
(18) Park, S. H.; Roy, A.; Beaupre, S.; Cho, S.; Coates, N.; Moon, J. S.; Moses, D.; Leclerc, M.; Lee, K.; Heeger, A. J. *Nat. Photonics* **2009**, *3*, 297−302.
(19) Xin, H.; Reid, O. G.; Ren, G.; Kim, F. S.; Ginger, D. S.; Jenekhe, S. A. *ACS Nano* **2010**, *4*, 1861−1872.
(20) Padinger, F.; Rittberger, R. S.; Sariciftci, N. S. *Adv. Funct. Mater.* **2003**, *13*, 85−88.
(21) Honda, S.; Nogami, T.; Ohkita, H.; Benten, H.; Ito, S. *ACS Appl. Mater. Interfaces* **2009**, *1*, 804−810.
(22) Li, G.; Yao, Y.; Yang, H.; Shrotriya, V.; Yang, G.; Yang, Y. *Adv. Funct. Mater.* **2007**, *17*, 1636−1644.
(23) Stevens, D. M.; Qin, Y.; Hillmyer, M. A.; Frisbie, C. D. *J. Phys. Chem. C* **2009**, *113*, 11408−11415.
(24) Tsoi, W. C.; Spencer, S. J.; Yang, L.; Ballantyne, A. M.; Nicholson, P. G.; Turnbull, A.; Shard, A. G.; Murphy, C. E.; Bradley, D. D. C.; Nelson, J.; Kim, J. S. *Macromolecules* **2011**, *44*, 2944−2952.
(25) Kozub, D. R.; Vakhshouri, K.; Orme, L. M.; Wang, C.; Hexemer, A.; Gomez, E. D. *Macromolecules* **2011**, *44*, 5722−5726.
(26) Bavel, S. S.; Sourty, E.; With, G.; Loos, J. *Nano Lett.* **2009**, *9*, 507−513.
(27) Chen, D.; Nakahara, A.; Wei, D.; Nordlund, D.; Russell, T. P. *Nano Lett.* **2011**, *11*, 561−567.
(28) Chen, D.; Liu, F.; Wang, C.; Nakahara, A.; Russell, T. P. *Nano Lett.* **2011**, *11*, 2071−2078.
(29) Yin, W.; Dadmun, M. *ACS Nano* **2011**, *5*, 4756−4768.
(30) Wu, W. R.; Jeng, U. S.; Su, C. J.; Wei, K. H.; Su, M. S.; Chiu, M. Y.; Chen, C. Y.; Su, W. B.; Su, C. H.; Su, A. C. *ACS Nano* **2011**, *5*, 6233−6243.
(31) Chiu, M. Y.; Jeng, U. S.; Su, C. H.; Liang, K. S.; Wei, K. H. *Adv. Mater.* **2008**, *20*, 2573−2578.
(32) Chen, H. Y.; Yang, H.; Yang, G.; Sista, S.; Zadoyan, R.; Li, G.; Yang, Y. *J. Phys. Chem. C* **2009**, *113*, 7946−7953.
(33) Sirringhaus, H.; Brown, P. J.; Friend, R. H.; Nielsen, M. M.; Bechgaard, K.; Langeveld-Voss, B. M. W.; Spiering, A. J. H.; Janssen, R. A. J.; Meijer, E. W.; Herwig, P.; Leeuw, D. M. *Nature* **1999**, *401*, 685−688.
(34) Moon, J. S.; Lee, J. K.; Cho, S.; Byun, J.; Heeger, A. J. *Nano Lett.* **2009**, *9*, 230−234.
(35) Moon, J. S.; Takacs, C. J.; Sun, Y.; Heeger, A. J. *Nano Lett.* **2011**, *11*, 1036−1039.
(36) Pfannmoller, M.; Flugge, H.; Benner, G.; Wacker, I.; Sommer, C.; Hanselmann, M.; Schmale, S.; Schmidt, H.; Hamprecht, F. A.; Rabe, T.; Kowalsky, W.; Schroder, R. R. *Nano Lett.* **2011**, *11*, 3099−3107.
(37) Herzing, A. A.; Richter, L. J.; Anderson, I. M. *J. Phys. Chem. C* **2010**, *114*, 17501−17508.
(38) Drummy, L. F.; Davis, R. J.; Moore, D. L.; Durstock, M.; Vaia, R. A.; Hsu, J. W. P. *Chem. Mater.* **2011**, *23*, 907−912.
(39) Yuan, M. C.; Chiu, M. Y.; Liu, S. P.; Chen, C. M.; Wei, K. H. *Macromolecules* **2010**, *43*, 6936−6938.
(40) Egerton, R. F. *Electron Energy-Loss Spectroscopy in the Electron Microscope*, 2nd ed.; Plenum Press: New York, 1996; Vol. 5, p 334.
(41) Popescu, L. M.; Hof, P.; Sieval, A. B.; Jonkman, H. T.; Hummelen, J. C. *Appl. Phys. Lett.* **2006**, *89*, 213507−1−213507−3.
(42) Chen, L. M.; Hong, Z.; Kwan, W. L.; Lu, C. H.; Lai, Y. F.; Lei, B.; Liu, C. P.; Yang, Y. *ACS Nano* **2010**, *4*, 4744−4752.
(43) Mauer, R.; Kastler, M.; Laquai, F. *Adv. Funct. Mater.* **2010**, *20*, 2085−2092.
(44) Yang, X.; Loos, J.; Veenstra, S. C.; Verhees, W. J. H.; Wienk, M. M.; Kroon, J. M.; Michels, M. A. J.; Janssen, R. A. J. *Nano Lett.* **2005**, *5*, 579−583.
(45) Ma, W.; Yang, C.; Heeger, A. J. *Adv. Mater.* **2007**, *19*, 1387−1390.
(46) Liu, H. J.; Jeng, U. S.; Yamada, N. L.; Su, A. C.; Wu, W. R.; Su, C. J.; Lin, S. J.; Wei, K. H.; Chiu, M. Y. *Soft Matter* **2011**, *7*, 9276−9282.
(47) Cheun, H.; Berrigan, J. D.; Zhou, Y.; Fenoll, M.; Shim, J.; Hernandez, C. F.; Sandhage, K. H.; Kippelen, B. *Energy Environ. Sci.* **2011**, *4*, 3456−3460.